Nanotechnology 31.36 (2020): 365704

DOI: https://doi.org/10.1088/1361-6528/ab96e5

Fabrication and characterization of nanostructured porous silicon-silver composite layers by cyclic deposition: dip-coating vs spin-coating

Nelson Naveas [1,2], Miguel Manso-Silván [1], Ruth Pulido [1,2], Fernando Agulló-Rueda [3], Vicente Torres-Costa [1], Tanya Plaza 4, Héctor Pesenti [4], Gonzalo Recio [4,5], Jacobo Hernández-Montelongo [4,6*]

Authors' addresses

[1] Departamento de Física Aplicada, Centro de Micro-Análisis de Madrid and Instituto de Ciencia de Materiales Nicolás Cabrera, Universidad Autónoma de Madrid, 28049, Madrid, Spain.

[2] Departamento de Ingeniería Química y Procesos de Minerales, Universidad de Antofagasta, Avenida Angamos 601, Antofagasta, Chile.

[3] Instituto de Ciencia de Materiales de Madrid (ICMM), CSIC, 28049, Madrid, Spain.

[4] Núcleo de Investigación en Bioproductos y Materiales Avanzados, UC Temuco, 47813312, Temuco, Chile.

[5] Facultad de Ingeniería y Tecnología, Universidad de San Sebastián, 4080871, Concepción, Chile

[6] Departamento de Ciencias Matemáticas y Físicas, UC Temuco, 4813302, Temuco, Chile.

* To whom correspondence should be addressed:

jacobo.hernandez@uct.cl

Abstract

Composites of nanostructured porous silicon and silver (nPSi-Ag) have attracted great attention due to the wide spectrum of applications in fields such as microelectronics, photonics, photocatalysis and bioengineering, Among the different methods for the fabrication of nanostructured composite materials, dip and spin-coating are simple, versatile, and cost-effective bottom-up technologies to provide functional coatings. In that sense, we aimed at fabricating nPSi-Ag composite layers. Using nPSi layers with pore diameter of 30 nm, two types of thin-film techniques were systematically compared: cyclic dip-coating (CDC) and cyclic spin-coating (CSC). CDC technique formed a mix of granular and flake-like structures of metallic Ag, and CSC method favored the synthesis of flake-like structures with Ag and Ag_2O phases. Flakes obtained by CDC and CSC presented a width of 110 nm and 70 nm, respectively. Particles also showed a nanostructure surface with features around 25 nm. According to the results of EDX and RBS, integration of Ag into nPSi was better achieved using the CDC technique. SERS peaks related to chitosan adsorbed on Ag nanostructures were enhanced, especially in the nPSi-Ag composite layers fabricated by CSC compared to CDC, which was confirmed by FTDT simulations. These results show that CDC and CSC produce different nPSi-Ag composite layers for potential applications in bioengineering and photonics.

Keywords: cyclic dip-coating; cyclic spin-coating; porous silicon; silver nanoparticles; composite material

1. Introduction

Currently, there is a huge interest in semiconductor-metal nanocomposites materials due to their interesting functional properties for different disciplines such as microelectronics,

photonics, photocatalysis, bioengineering, among others [1, 2]. When semiconductors are combined with noble metals, their properties can significantly change. For instance, processes such as enhanced charge separation at the semiconductor-metal interface and the enhanced visible light absorption caused by the surface plasmon resonance (SPR) of metals can improve the photocatalytic properties of semiconductors [1]. In particular, composites of nanostructured porous silicon (nPSi) and silver (Ag) have attracted great attention because of their wide spectrum of applications, such as in gas and biological sensors, catalysis and optoelectronics. Their properties come along with the low-cost of material production and the compatibility with complementary metal-oxide-semiconductor technology (CMOS) [3, 4].

nPSi is a very attractive semiconductor material which consists of silicon nanocrystals embedded in a porous amorphous matrix [5, 6]. It elicits as an efficient substrate for fabricating semiconductor-metal composites because it shows a large surface area (200-500 $m^2 \cdot cm^{-3}$) [5], biocompatibility, along with simple fabrication methods. Likewise, nPSi surfaces can be easily modified by using diverse chemical and physical methods. Meanwhile, the interesting properties of Ag nanoparticles make them perfect for the application as an antimicrobial agent, biosensor materials, composite fibers, cryogenic superconducting materials, cosmetic products, and electronic components [7, 8].

In that sense, several methods have been performed to obtain nPSi-Ag composites for different applications. Giorgis et al. (2009) [9] achieved nPSi-Ag nanoparticles composite with thermal decomposition of $AgNO_3$ at 500 ºC, which presented potential uses as Surface Enhanced Raman Scattering (SERS) substrate. On the other hand, Ensafi et al. (2016) [10] synthetized nPSi-Ag composite by galvanic replacement reaction between Si atoms in the nPSi and Ag cation in aqueous HF solution. The obtained composite was

tested as an electrochemical sensor platform of H_2O_2. Using the same method, Skrabic et al. (2019) [11] reacted nPSi layers with an Ag precursor solution at different concentrations and times. The obtained nPSi-Ag composites were tested as SERS photonic crystals. Regarding the electrochemical deposition, Spivak (2018) [12] used different kinds of nPSi to grow Ag into the pores. Spivak reported that the increase of deposition time led to changes in Ag morphology and proposed these nPSi-Ag composites for catalysis and plasmonic applications. Also, Martín-Palma et al. (2019) [3] have grown Ag particles inside the nPSi structure by electrochemical deposition. The authors obtained a homogeneous distribution of Ag nanoparticles on the surface and inside the nPSi layer. These composites were tested as wideband optical absorbers for photonic and plasmonic applications. Even by metal assisted chemical etching, Ge et al obtained different Ag nanostructure on nPSi layer by changing the $AgNO_3$ concentration in the electrochemical solutions with SERS effects [13]. In general, the selected method to deposit Ag on nPSi layers can directly affect the physicochemical properties of the composite, such as the morphology, thickness, and homogeneity, which can impact the material performance in specific applications.

Among the different methods for the fabrication of such nanostructured composites, dip and spin-coating are interesting bottom-up technology to provide functional thin-film coatings. In fact, these techniques are simple, versatile, and cost-effective for this purpose. Moreover, both techniques can be performed at atmospheric conditions, and interestingly, each technique can produce specific morphologies and phases, even using the same stem-solutions [14]. The dip-coating technique consists in the substrate immersion into a reservoir of the coating suspension to deposit a layer of material upon withdrawal. This method can provide thin films as required, and this is easily controllable with the

concentration of the suspension used [15]. On the other hand, in the spin-coating technique, a diluted suspension is placed on the substrate and rotated at high speed, while the fluid spins off the edges coating the substrate at the same time that the solvent evaporates. Spin-coating is widely used for the production of very thin films (below 10 μm) [15].

In this regard, the novelty of this work is the fabrication of nPSi-Ag composite layers by systematically comparing two types of thin-film techniques, namely, cyclic dip-coating (CDC) and cyclic spin-coating (CSC). Both techniques CDC and CSC, consist of a series of Ag deposition steps on nPSi. The CDC technique is applied by cycling the immersion of nPSi substrate into an Ag^+ solution, while the CSC method consists in repeating cycles of centrifugal dispersion of an Ag^+ solution on nPSi. Although dip-coating and spin-coating have been used in diverse substrates, as it was previously explained, they have not been used to obtain nPSi-Ag composites. Moreover, our proposals are based on repetitive cycles. The two nPSi-Ag composite layers obtained by CDC and CSC were characterized in terms of morphology, infiltration (depth profiling) of Ag into the nPSi, crystallinity, chemical composition and optical characteristics. Interestingly, we aim at highlighting the structural and functional properties of the different nPSi-Ag composite layers even if obtained by using the same nPSi substrate and Ag^+ stem-solution at room temperature. In that sense, the main differences between the composites fabricated with both experimental techniques were in detail analyzed.

2. Experimental Approach

2.1 Fabrication of nPSi

Nanostructured porous silicon (nPSi) substrates (3 cm^2) were fabricated galvanostatically by photoassisted electrochemical etching of single-crystalline p-type Si wafers (boron-

doped, orientation <100>), resistivity 0.001–0.005 Ω·cm) in a 1:2 solution of 48% HF and 98% ethanol. The applied current density was set to 80 $mA \cdot cm^{-2}$ during 120 under illumination with a 150 W halogen lamp. Light is used just to create pairs electron-holes in the silicon substrate. This effect forms more homogeneous layers because the etching begins when holes reach the silicon surface and react with F^- ions.

The as-prepared nPSi layers were stabilized by a chemical oxidation process in H_2O_2 (30% v/v) overnight, as previously reported [16]. Finally, nPSi substrates were dried under nitrogen streamflow and used as the template for Ag deposition. Si wafers were purchased from University Wafer, South Boston, USA, and chemical products were acquired from Merck, Santiago, Chile.

2.2 Formation of the nPSi-Ag composite layers

In order to fabricate the nPSi-Ag composite layers, a highly diluted chitosan solution, as a stabilizer, was prepared at 1 mg/100 ml adding glacial acetic acid at 100 mM by stirring overnight (chitosan of low molecular weight ≈ 5×104 g/mol, 75–85% deacetylated, and ultrapure water Mili-Q system; 18.2 M Ω·cm). Then, AgNO3 salt was dissolved in this solution at a concentration of 1 mM and adjusted to pH = 4.0 using 0.1 M NaOH solution.

For the deposition process, one of two thin-film techniques were used: (i) cyclic dip-coating (CDC) or (ii) cyclic spin-coating (CSC), respectively. The standard deposition for the CDC series comprised the immersion of nPSi substrates in the $AgNO_3$ solution for 10 min and a consecutive cleaning in ultrapure water for an equivalent time. The pH of rinsing water was previously adjusted to 4. Likewise, the deposition was repeated for 3, 6, 9, and 12 cycles in a row. On the other hand, the standard deposition for the CSC series

consisted of alternating 500 μL of $AgNO_3$ solution and the same quantity of ultrapure water onto the nPSi substrate at 3000 rpm during 60 s. This process was repeated for 3, 6, 9, and 12 cycles in a row. For both techniques, after samples were obtained at different cycles, they were immersed into 1 mM ascorbic acid solution for 3 h in order to reduce the ionic silver and to stabilize the silver nanoparticles. Finally, the samples were washed with ultrapure water and dried at room temperature. All chemical products were acquired from Merck, Santiago, Chile.

2.3 Characterization techniques

Morphological characterization of nPSi-Ag composites layers has been carried out by field-emission scanning electron microscopy (FESEM; Philips XL-40FEG), operating with an acceleration potential of 10 keV. The size distribution of Ag particles was presented as histograms; data were obtained from the FESEM images that were processed using freely available ImageJ software.

In-depth profiling of the Ag particle infiltration into nPSi layers was studied using both semiquantitative chemical information by energy dispersive X-ray analysis (EDX) and Rutherford Backscattering Spectroscopy (RBS). EDX was acquired with a Hitachi S-3000N scanning electron microscope. RBS experiments were carried out at the standard beamline at the 5 MV Cockroft-Walton tandetron accelerator of the Centro de Micro-Análisis de Materiales (CMAM). For the measurements, 2 MeV He^+ ions were used. The scattered ions were detected at a scattering angle of 170º with a Si semiconductor particle detector; the samples were oriented in random geometry to avoid channeling through the crystalline substrate. The vacuum was about 5 10–5 Pa. Simulations and spectra fitting was carried out using the software SIMNRA 7.02.

Crystallographic structures of the Ag particles deposited on nPSi by both techniques were examined by X-ray Diffraction (XRD) using a Rigaku X-ray diffractometer Smartlab model, with goniometer Theta-Theta Bragg-Brentano geometry and solid-state detector D/teX Ultra 250 model (Rigaku Corporation, Japan). The instrumental alignment was checked against the NIST SMR 660c LaB6 powder standard and its optic configuration was employed Ni-filtered Cu radiation (30 kV and 40 mA), 0.5° divergence slit, 0.25° anti-scatter slit, and both sides with 5° Soller slits. In preference, patterns were collected in the 20–60° range, counting 0.5°/sec per step of 0.01°. PDXL 2 v.2.7.3.0 software and ICDD 2018 PDF-4 reference database were used for search match phases. The crystallite size estimation of the Ag nanoparticles was done using the Williamson-Hall plot Method [17].

Raman spectra were acquired at room temperature using a Renishaw Ramascope 2000 microspectrometer, equipped with point by point spectral mapping (confocal with lateral and depth resolution) and a 514.5 nm excitation wavelength (green) line from an argon-ion laser. Exciting light was focused on the sample surface with a BH-2 Olympus microscope. The objective had a 50 X magnification and a numerical aperture of NA = 0.85. The laser power on the sample surface was of the order of 1 mW. The integration time for each CCD pixel was 50 s. The error in the Raman shift was smaller than 0.5 cm^{-1} and the spectral resolution of about 3 cm^{-1}.

Finite Difference Time Domain (FDTD) simulations were carried out using commercial FDTD Solutions software from Lumerical Solutions Inc., (Vancouver, Canada). The final structure PSi-Ag was modelled as a silver nano-flake with a cylindrical shape and a ratio of radius/height set to 0.25 laid on a flat silicon substrate of dimension 500 nm x 500 nm x 150 nm. The diameter of Ag nanoflakes was changing from 60 nm to 120 nm. In addition, a gap of 1 nm between Ag nanoflakes and Si substrate was added in

order to simulate the space for biomolecules, which induced enhanced Raman intensity. PML (Perfectly matched layer) were used as boundary conditions. The propagation direction of plane waves (wavelength of 515 nm) was placed along z direction. The local electrical field was computed for each mesh, and the final field intensity relative to the excitation field E_0 was evaluated.

3. Results and discussion

In this study, single nPSi layers obtained by electrochemical anodization of silicon wafers were chosen as semiconductor substrates for the deposition of Ag particles, and consequently, the obtention of semiconductor-metal composites. Figure 1 shows a fabrication scheme of the nPSi-Ag composite layers. Figure 1a presents the synthesis of nPSi substrates by photoassisted electrochemical etching, followed by stabilization of its porous structure trough chemical oxidation with H_2O_2. Additionally, Figure 1b and Figure 1c show a schematic representation of the CDC and CSC techniques, respectively. In the CDC method, the obtained nPSi substrate was cyclically dipped into an $AgNO_3$ solution, where Ag^+ is formed. In the case of the CSC technique, the Ag^+ solution was cyclically deposited on the nPSi substrate by spin-coating. For both techniques, samples were obtained after a different number of cycles and immersed in an ascorbic acid solution in order to reduce Ag^+ ions to Ag^0.

It has been reported that the deposition of metals onto nPSi layers is strongly influenced by the etching conditions of the nPSi along with the concentration of the metal solution and the duration of the deposition [9, 11, 18]. In that sense, Figures 2a and 2b present the surface and cross-sectional FESEM views, respectively, of a standard nPSi layer used in this work. As can be seen, the nPSi layer is characterized by column-like porous

morphology with an average pore diameter of 30 nm (black regions of Figure 2a) and a layer thickness of 10 μm (Figure 2b). This type of nPSi material offers the optimal features of porosity and high surface area for proper surface functionalization and/or nucleation of noble metals [19], such as Ag nanoparticle.

The mechanism of Ag deposition onto nPSi layers began firstly with the role of chitosan solution (section 2.2). Generally, metal nanoparticles aggregate among themselves and progressively grow into larger clusters, which eventually precipitate. Therefore, the use of stabilizers is necessary [20-22]. Chitosan, as a natural polysaccharide, is an environmentally benign, biodegradable, highly abundant and low cost, which is more favorable to be utilized as a stabilizer for synthesized Ag nanoparticles than synthetic polymers [21]. The stabilization faculty of chitosan is due to its sorption abilities and capacity to form chelate compounds with metal ions, such as Ag^+ [22]. Afterward, the reduction of Ag^+ ions to Ag^0 was due to the presence of the antioxidative ascorbic acid. Ascorbic acid can reduce and thereby neutralize, reactive species leading to the formation of ascorbate radical and electrons transfer. The reaction involves the transfer of two electrons and the formation of dehydroascorbic acid. These free electrons reduce the 2 Ag^+ ions to metallic 2 Ag^0 [23, 24]. The mechanism is summarized as follows:

$$AgNO_3 \rightarrow Ag^+ + NO_3^- \quad (1)$$

$$2Ag^+ + \text{ascorbic acid} \rightarrow \text{dehydroascorbic acid} + Ag^0 + 2H^+ \quad (2)$$

In our case, the deposition of Ag was performed under dark conditions to avoid Ag formation by photoreduction of metal ions present in the solution, due to the reductive action of nPSi [25].

Figure 3 shows FESEM images of the surface and cross-section of typical nPSi-Ag composite layers fabricated by CDC and CSC after 12 cycles. Both techniques resulted in a homogeneous islands-like deposition (Figure 3a for CDC, and Figure 3e for CSC). Ag particles obtained by CDC (Figures 3b and 3c) exhibited two kinds of morphology: granular and flake-like structure, in a proportion of 44% and 56%, respectively. Moreover, the obtained distribution size of these particles (Figure 3i) presented an average length of 0.7 and 1.4 μm for the granular and flakes-like particles, respectively. In the latter, flakes that showed a random orientation had an average width of 110 nm (Figure 3k). In Figure 3c, it is possible to observe that both kinds of Ag particles presented surface features of nanoclusters of around 25 nm. Finally, the Ag deposition performed by CDC reached up an average thickness of 1 μm (Figure 3d). In the case of the Ag deposition obtained by CSC (Figure 3f and 3g), particles showed a predominant flake-like morphology, and most of them were in a horizontal (#1 of Figure 3g) and vertical (#2 of Figure 3g) orientation. In fact, some flakes in horizontal position were superimposed onto each other. The size of these particles was considerably smaller than the ones obtained by the CDC. According to its corresponding distribution size (Figure 3j), they exhibited an average length of 0.3 μm, and a smaller width than CDC: an average of 70 nm in its distribution size (Figure 3l). Moreover, the deposition led to a thickness lower than with CDC, reaching up just an average of 0.5 μm.

In order to get a clearer picture of the Ag distribution, we used SEM-EDX in cross-section and RBS analysis to identify the potential diffusion and nucleation of Ag in-depth. Figure 4 shows SEM images and the relative concentration profile of Ag in the cross-section of nPSi-Ag composite layer obtained by EDX. The deposition of Ag does not only occur at the nPSi surface but also inside the pores of the column-like porous structure. The

concentration-depth chart for Ag shows the presence of different diffusion profiles for nPSi-Ag composite layers fabricated by CDC and CSC. In general, CDC (Figure 4a) allows more infiltration of the Ag nanoparticles into the nPSi layers than CSC (Figure 4b). In the case of CDC, Ag concentration was considerably increased with the number of deposition cycles. For example, in the first micron of depth, Ag% was increased from 3% to 10% by increasing the number of cycles from 3- to 12-cycles, respectively. Besides, at the bottom of the nPSi layer (at 10 μm), Ag% was increased from 0.6% to 3.3% with 3- and 12-cycles, respectively. However, for the case of CSC, Ag deposition was more superficial, showing only slight differences in Ag infiltration with the number of cycles. In the first microns of depth, Ag% increased from 3% to 5% with 3- and 12-cycles, respectively. However, on the bottom of nPSi substrate, Ag% was around 0.5% for both samples.

After assessing the diffusion of Ag inside the porous layer by EDX, RBS measurements were performed to obtain higher precision compositional profiles of both CDC and CSC samples and study the penetration of Ag inside nPSi in greater detail. Figure 5 shows the experimental and simulated RBS spectra of a typical nPSi-Ag composite layer fabricated by CDC and CSC after 12 cycles on identical nPSi substrates. In both spectra, the signals corresponding to Ag and Si are clearly differentiated, while that of O appears superimposed to the Si signal. Both the CDC and CSC samples show an Ag signal that extends from its surface position to lower energy channels, indicating that Ag is indeed infiltrated into the nPSi layer. Interestingly, the Ag signal extends further to lower energies in CDC than CSC, suggesting a deeper infiltration of Ag. Figure 6 shows the in-depth concentration profile determined from the spectra fit. The profiles show a surface Ag concentration of 0.14 and 0.11 for the CDC and CSC samples, respectively. Silicon is also detected at its surface energy, indicating that the nPSi surface is not completely covered by

Ag, but instead, Ag islands grow on top of the nPSi surface [14], as already revealed by the FESEM images. In the case of CDC, Ag concentration gradually decreases from 0.14 atomic content down to 0.025 at a depth of 13000×1015 at/cm^2, corresponding to the bottom of the nPSi layer (i.e., the nPSi/Si interface). Conversely, the Ag concentration of the sample fabricated by CSC decreases below an undetectable level at a depth of 5900×1015 at/cm^2, indicating that in this case, the Ag infiltration did not reach the nPSi/silicon interface. These results are in good agreement with those obtained by EDX, provided that the lower spatial resolution of EDX is taken into account. Both techniques, EDX and RBS, showed the infiltration of Ag into the nPSi structure and confirmed that the CDC technique provides a higher and deeper infiltration than CSC. This was because, according to the deposition method (dipping, spinning, electrodeposition, etc.), different driving forces are playing a key role in the film formation [26]. In our case, a possible explanation for our results is that CDC was dominated by viscous forces, unlike the CSC technique, where centrifugal forces play a key role.

In order to characterize the crystalline nature of the nPSi-Ag composite layers, we analyzed the samples by XRD. Figure 7 shows the XRD pattern of nPSi-Ag composite layers using CDC and CSC techniques. For both cases, the peak intensity increased with the number of deposition cycles. In the case of CDC (Figure 7a), metallic Ag (fcc structure) with characteristic (111) plane and low intensity of the (200) plane were detected at 38.11º and 44.29º, respectively. Due to the high intensity of the (111) lattice plane, Ag particles shall be oriented along this direction parallel to the supporting nPSi substrate. Moreover, as the obtained peaks were sharp and with high intensity, good crystallinity of the synthesized Ag particles was confirmed. On the other hand, based on particle size by XRD pattern profile analysis, the Ag presents an average crystallite size of 24 nm, which suggests an

internal nanostructure in the Ag clusters. Regarding the nPSi-Ag composite layers obtained by CSC (Figure 7b), they exhibited the same metallic Ag with characteristic (111) plane and little intensity of (200) plane at 38.11º and 44.29º, respectively. However, an additional peak was detected at 33.02º, which corresponds to (111) plane of silver oxide. As in the previous case, (111) planes also showed a high intensity suggesting that (111) planes of Ag and Ag_2O particles were dominantly oriented parallel to the supporting nPSi substrate. Based on particle size analysis of XRD pattern, the synthesized Ag and Ag_2O particles should present an average particle size of 20 nm. It is important to highlight that particle sizes determined by XRD profile are in the order of the nanostructure pattern previously observed by FESEM on surface Ag particles. In that sense, this can also explain the presence of Ag_2O in CSC. As particles obtained by CSC technique were considerable smaller than CDC (see histograms of Figure 3), this means that the surface area/volume ratio of particles in CSC was higher than CDC, what made them more reactive with the oxygen from the air, and therefore, generated the Ag_2O phase in the silver particles. Finally, another important issue is the intensity of the peaks related to each Ag nucleation technique (Figure 7c). Peaks obtained from CDC samples are 8 times more intense than CSC samples. This is directly related to the amount of Ag deposited on samples.

Figure 8 shows the Raman spectra of nPSi-Ag composite layers using CDC and CSC techniques. All samples exhibited a strong, sharp and asymmetrically broadened peak near to 514 cm^{-1} due to the optical phonon mode of silicon nanocrystals in nPSi. Also, two broad peaks, which are assigned to Ag nanostructures-induced SERS of chitosan, were found in all nPSi-Ag composite layers. These peaks came from the chitosan used as a stabilizer in the Ag^+ stem-solution. Thus, assignments to scissoring bending vibrations of C–H and $–NH_2$ groups of chitosan were detected (δ(C–H) and δ(NH2), respectively. δ(C–

H) was detected in the peaks at 1380 cm^{-1} for CDC, and 1376 cm^{-1} for CSC [27, 28]. $\delta(NH_2)$ was identified in the peaks at 1590 cm^{-1} and 1589 cm^{-1} for CSD and CSC, respectively [27, 28]. Interestingly, these peaks were enhanced for the samples fabricated at 9 and 12 cycles, especially in the nPSi-Ag composite layers fabricated by CSC. This can be explained by the smaller width of CSC flakes against CDC flakes: 70 nm versus 110 nm; thinner particles enhance the Raman scattering of a molecule situated in the vicinity of nano-sized metallic structures [29]. Similar peaks have been reported for Ag-porous silicon [30]. In fact, these peaks assigned to Ag-nanostructures-induced SERS were attributed to adsorbed organic molecules on Ag nanoparticles, such as Rhodamine 6G dye [31], biomolecules [32] and pyridine [33]. Figure 9 shows a detailed view of the Raman spectra of the silicon one-phonon line of nPSi-Ag composite layers using both techniques: CDC and CSC. Compared to the spectrum of bulk silicon (optical phonon mode at 521 cm^{-1}), the spectrum of nPSi was shifted and broadened towards lowers frequencies due to the quantum confinement effect of silicon nanocrystals [34, 35]. To estimate the average size of the silicon nanocrystals, we have used the formula $\Delta\nu = - A(a/D)^{\gamma}$ obtained by Zi et al. [36] for spherical nanocrystals using a bond polarizability model. D is the average diameter, $\Delta\nu = \nu(D) - \nu(\text{bulk})$ is the shift of the Raman peak with respect to bulk silicon, a = 0.543 nm is the silicon cell parameter, A = 47.41 cm^{-1} and γ = 1.44. For CDC samples, the observed peak shift $\Delta\nu$ = -6.5 cm^{-1} corresponds to an average diameter of about 2 nm. For CSC samples, it is -9.2 cm, which corresponds to an average diameter of 1.7 nm. The reduction of the silicon nanocrystal size for CSC samples can be explained by further oxidation of the samples. The important point here is the general trend of the average size of the nanocrystals rather than the absolute values because there are many factors and

different models that can affect the precise value of the estimated size, as has been discussed before in the literature [37].

In order to get a deeper knowledge about SERS observation, finite difference time-domain (FDTD) simulations were performed. FDTD method allows solving Maxwell's equations on a discrete spatial grid [38]. nPSi-Ag composites were modelled as an Ag nanoflake with different diameters on a flat silicon substrate with a gap of 1 nm between both objects (further details in the experimental section). The propagation direction of light with a wavelength of 515 nm was set along z axis, while the Ag nanoflake was placed parallel to the substrate. Cross-section maps of computed intensity for an Ag nanoflake of 80 nm of diameter are represented in Figures 10a and 10b for z-x and z-y planes, respectively. It can be observed a high enhancement of the EM filed in the gap between Ag nanoflake and Si substrate (Figure 10a), which is more intensive at the ends of the Ag nanoflake (Figure 10b). In particular, in Figure 10a two different "hot sites" placed near the center of the nanoflakes with a high factor enhancement can be observed. Similar results have been reported for other kinds of metal nanostructures [39-41]. These sites can be responsible for SERS effects observed in the nPSi-Ag composites. In Figure 10 c, the intensity distribution in the middle of the gap between Ag nanoflake and Si substrate was plotted as a function of the distance from the middle of the Ag nanoflake. The intensity was explored for 4 different Ag nanoflakes with different diameters. It can be observed the two "hot sites" for all the diameters. These sites presented their maximum enhancement around 5 nm from the center of the nanoflakes, and they totally disappear around 25 nm away from the center. These results indicate that the "hot sites" for SERS are very limited in the composite. This can be the reason because CSC composite shows a higher enhancement of

chitosan Raman signal compared to CDC composite, although CDC composites present a higher amount of Ag nanostructures.

The experimental results showed that CDC and CSC can be optimal techniques to produce nPSi-Ag composites for optoelectronic and biosensing applications. Firstly, photoassisted electrochemical etching of silicon wafer allows controlling the final layer of nPSi without the needed of deposited any metal in the top of silicon wafers, as the case of metal assisted chemical etching method [42]. Besides, more homogeneous layers are synthetized. nPSi obtained by photoassisted electrochemical etching is also a faster technique than other techniques, such as laser assisted chemical etching [43], and considerable higher areas of nanostructured Si can be obtained. In comparison with techniques to deposit Ag nanostructure on nPSi, CDC and CSC allow obtaining Ag nanostructures without high energy consumption such as thermal decomposition [9] because CDC and CSC are techniques operated at in room temperature conditions. Although electrochemical deposition [3] is also a room-temperature technique, it usually perfumes a thin layer of silver on the top of nPSi, while CDC and CSC have shown that Ag nanostructured not completely covers the surface of nPSi, with can better fix for some applications such as SERS substrate and biosensing.

4. Conclusion

In the present study, nanoporous silicon (nPSi)-Ag composites layers were fabricated by two types of thin-film techniques and systematically compared: cyclic dip-coating (CDC) and cyclic spin-coating (CSC). Firstly, nPSi layers obtained by photoassisted electrochemical etching of silicon wafers presented pores diameter of 30 nm. Regarding the cyclic deposition techniques, each process produced specific morphologies and Ag phases

using the same Ag^+ stem-solution. CDC technique formed a mix of granular and flake-like structures of metallic Ag. Instead, CSC favored the synthesis of flake-like structures with Ag and Ag_2O phases. Flakes obtained by CDC and CSC presented a width of 110 nm and 70 nm, respectively. Particles also showed a nanostructure surface with features around 25 nm. Moreover, according to the results of EDX and RBS, integration of Ag into nPSi porous structure was better achieved using CDC technique. On the other hand, surface-enhanced Raman scattering (SERS) peaks related to chitosan adsorbed on Ag nanostructures were enhanced, especially in the nPSi-Ag composite layers fabricated by CSC. All these differences in the nPSi-Ag composite layers obtained depending on the performed process of synthesis can be of interest for potential applications in bioengineering and photonics as SERS-based sensors.

Acknowledgments

This work was financially supported by Fondo Nacional de Desarrollo Científico y Tecnológico FONDECYT–Chile (grant number 11180395), FONDEQUIP–Chile (project 160152), CONICYT PFCHA/DOCTORADO/2017-21172001 (Nelson Naveas) and PFCHA/DOCTORADO/2015-21151648 (Ruth Pulido).

Authors contributions

NN and JHM conceived and designed experiments; NN and GR synthetized the nPSi substrates; NN, RP and TN synthetized both kind of composites; NN and MMS performed the FESEM and SEM-EDX characterization; VTC performed the RBS characterization; HP performed the XRD characterization; FAR performed the Raman characterization; GR performed the FDTD simulations; NN and JHM analyzed the data; NN, MMS and JHM

contributed reagents/materials/analysis tools; NN and JHM wrote the manuscript. All authors revised the manuscript.

Declaration of interest statement

The authors declare that they have no competing interests.

References

[1] Semenova D, Gernaey K V and Silina Y E 2018 Exploring the potential of electroless and electroplated noble metal–semiconductor hybrids within bio- and environmental sensing *Analyst* **143** 5646-69

[2] Fu Y-s, Li J and Li J 2019 Metal/Semiconductor Nanocomposites for Photocatalysis: Fundamentals, Structures, Applications and Properties *Nanomaterials* **9**

[3] Martín-Palma R J, McAtee P D, Ramadan R and Lakhtakia A 2019 Hybrid Nanostructured Porous Silicon-Silver Layers for Wideband Optical Absorption *Scientific Reports* **9** 7291

[4] Nativ-Roth E, Rechav K and Porat Z e 2016 Deposition of gold and silver on porous silicon and inside the pores *Thin Solid Films* **603** 88-96

[5] Hernández-Montelongo J, Muñoz-Noval A, García-Ruíz J P, Torres-Costa V, Martín-Palma R J and Manso-Silván M 2015 Nanostructured porous silicon: the winding road from photonics to cell scaffolds - a review *Frontiers in bioengineering and biotechnology* **3** 60-

[6] Zhang T, Wu S, Xu J, Zheng R and Cheng G 2015 High thermoelectric figure-of-merits from large-area porous silicon nanowire arrays *Nano Energy* **13** 433-41

[7] Aboelfetoh E F, El-Shenody R A and Ghobara M M 2017 Eco-friendly synthesis of silver nanoparticles using green algae (Caulerpa serrulata): reaction optimization, catalytic and antibacterial activities *Environmental Monitoring and Assessment* **189**

[8] Verma P and Maheshwari S K 2019 Applications of Silver nanoparticles in diverse sectors *International Journal of Nano Dimension* **10** 18-36

[9] Giorgis F, Virga A, Descrovi E, Chiodoni A, Rivolo P, Venturello A and Geobaldo F 2009 SERS-active substrates based on silvered porous silicon *physica status solidi c* **6** 1736-9

[10] Ensafi A A, Rezaloo F and Rezaei B 2016 Electrochemical sensor based on porous silicon/silver nanocomposite for the determination of hydrogen peroxide *Sensors and Actuators B: Chemical* **231** 239-44

[11] Škrabić M, Kosović M, Gotić M, Mikac L, Ivanda M and Gamulin O 2019 Near-Infrared Surface-Enhanced Raman Scattering on Silver-Coated Porous Silicon Photonic Crystals *Nanomaterials* **9**

[12] Spivak Y 2018 Porous Silicon as a Material for Nanocomposites and the Effect of its Parameters on the Morphology of Silver Clusters. In: *2018 IEEE International Conference on Electrical Engineering and Photonics (EExPolytech),* pp 244-8

[13] Ge D, Wei J, Ding J, Zhang J, Ma C, Wang M, Zhang L and Zhu S 2020 Silver Nano-Dendrite-Plated Porous Silicon Substrates Formed by Single-Step Electrochemical Synthesis for Surface-Enhanced Raman Scattering *ACS Applied Nano Materials* **3** 3011-8

[14] Hernandez-Montelongo J, Gallach D, Naveas N, Torres-Costa V, Climent-Font A, Garcia-Ruiz J P and Manso-Silvan M 2014 Calcium phosphate/porous silicon biocomposites prepared by cyclic deposition methods: Spin coating vs

electrochemical activation *Materials Science & Engineering C-Materials for Biological Applications* **34** 245-51

[15] Herrera M A, Sirviö J A, Mathew A P and Oksman K 2016 Environmental friendly and sustainable gas barrier on porous materials: Nanocellulose coatings prepared using spin- and dip-coating *Materials & Design* **93** 19-25

[16] Guzmán-Oyarzo D, Plaza T, Recio-Sánchez G, Abdalla S P D, Salazar A L and Hernández-Montelongo J 2019 Use of nPSi-βCD Composite Microparticles for the Controlled Release of Caffeic Acid and Pinocembrin, Two Main Polyphenolic Compounds Found in a Chilean Propolis *Pharmaceutics* **11**

[17] Williamson G K and Hall W H 1953 X-ray line broadening from filed aluminium and wolfram *Acta Metallurgica* **1** 22-31

[18] Alwan A M, Yousif A A and Wali L A 2018 A Study on the Morphology of the Silver Nanoparticles Deposited on the n-Type Porous Silicon Prepared Under Different Illumination Types *Plasmonics* **13** 1191-9

[19] Juneau-Fecteau A and Fréchette L G 2018 Tamm plasmon-polaritons in a metal coated porous silicon photonic crystal *Optical Materials Express* **8** 2774-81

[20] Cinteza O L, Scomoroscenco C, Voicu N S, Nistor L C, Nitu G S, Trica B, Jecu M-L and Petcu C 2018 Chitosan-Stabilized Ag Nanoparticles with Superior Biocompatibility and Their Synergistic Antibacterial Effect in Mixtures with Essential Oils *Nanomaterials* **8**

[21] Hettiarachchi M and Wickramarachchi S 2012 Synthesis of chitosan stabilized silver nanoparticles using gamma ray irradiation and characterization *Journal of Science of the University of Kelaniya Sri Lanka* **6**

[22] Elbarbary A M and El-Sawy N M 2017 Radiation synthesis and characterization of polyvinyl alcohol/chitosan/silver nanocomposite membranes: antimicrobial and blood compatibility studies *Polymer Bulletin* **74** 195-212

[23] Isaac R S R, Sakthivel G and Murthy C 2013 Green Synthesis of Gold and Silver Nanoparticles Using Averrhoa bilimbi Fruit Extract *Journal of Nanotechnology* **2013** 6

[24] Patra S, Sen D, Pandey A K, Bahadur J, Mazumder S, Ramagiri S V, Bellare J R, Roth S V, Santoro G, Yu S and Goswami A 2014 Time resolved growth of membrane stabilized silver NPs and their catalytic activity *RSC Advances* **4** 59379-86

[25] Recio-Sánchez G, Namura K, Suzuki M and Martín-Palma R J 2014 Nanostructured copper/porous silicon hybrid systems as efficient sound-emitting devices *Nanoscale Research Letters* **9** 487

[26] Richardson J J, Björnmalm M and Caruso F 2015 Technology-driven layer-by-layer assembly of nanofilms *Science* **348** aaa2491

[27] Zając A, Hanuza J, Wandas M and Dymińska L 2015 Determination of N-acetylation degree in chitosan using Raman spectroscopy *Spectrochimica Acta Part A: Molecular and Biomolecular Spectroscopy* **134** 114-20

[28] Ren X D, Liu Q S, Feng H and Yin X Y 2014 The Characterization of Chitosan Nanoparticles by Raman Spectroscopy *Applied Mechanics and Materials* **665** 367-70

[29] Hernández-Arteaga A C, Delgado-Nieblas F C, Ojeda-Galván H J, Velázquez-Salazar J J, Vinogradova E, José-Yacamán M, Guirado-López R A and Navarro-Contreras H R 2017 Surface-Enhanced Raman Spectroscopy of Acetil-neuraminic

Acid on Silver Nanoparticles: Role of the Passivating Agent on the Adsorption Efficiency and Amplification of the Raman Signal *The Journal of Physical Chemistry C* **121** 21045-56

[30] Naddaf M, Al-Mariri A and Haj-Mhmoud N 2017 Characterization of Ag-porous silicon nanostructured layer formed by an electrochemical etching of p-type silicon surface for bio-application *Materials Research Express* **4** 065013

[31] Zhong F, Wu Z, Guo J and Jia D 2018 Porous Silicon Photonic Crystals Coated with Ag Nanoparticles as Efficient Substrates for Detecting Trace Explosives Using SERS *Nanomaterials* **8**

[32] Yang W, Li Z, Lu Z, Yu J, Huo Y, Man B, Pan J, Si H, Jiang S and Zhang C 2019 Graphene-Ag nanoparticles-cicada wings hybrid system for obvious SERS performance and DNA molecular detection *Optics Express* **27** 3000

[33] Hara R, Fukuoka T, Takahashi R, Utsumi Y and Yamaguchi A 2015 Surface-enhanced Raman spectroscopy using a coffee-ring-type three-dimensional silver nanostructure *RSC Advances* **5** 1378-84

[34] Ivanda M 2018 *Handbook of Porous Silicon,* ed L Canham (Cham: Springer International Publishing) pp 611-20

[35] Wolf I D 1999 Stress measurements in Si microelectronics devices using Raman spectroscopy *Journal of Raman Spectroscopy* **30** 877-83

[36] Zi J, Büscher H, Falter C, Ludwig W, Zhang K and Xie X 1996 Raman shifts in Si nanocrystals *Applied Physics Letters* **69** 200-2

[37] Mavi H, Shukla A K, Kumar R, Rath S, Joshi B and Islam S s 2006 Quantum confinement effects in silicon nanocrystals produced by laser-induced etching and cw laser annealing *Semiconductor Science and Technology* **21** 1627-32

[38] Sullivan D 2013 Electromagnetic Simulation Using the FDTD Method, Second Edition *IEEE Microwave Theory Tech Soc*

[39] Kim K, Shin D, Kim K L and Shin K S 2012 Surface-enhanced Raman scattering of 4,4′-dimercaptoazobenzene trapped in Au nanogaps *Physical Chemistry Chemical Physics* **14** 4095-100

[40] Kim K, Lee H B and Shin K S 2013 Surface-enhanced Raman scattering characteristics of nanogaps formed by a flat Ag substrate and spherical Pt nanoparticles *Spectrochimica Acta Part A: Molecular and Biomolecular Spectroscopy* **100** 10-4

[41] Kim M, Ko S M, Kim J-M, Son J, Lee C, Rhim W-K and Nam J-M 2018 Dealloyed Intra-Nanogap Particles with Highly Robust, Quantifiable Surface-Enhanced Raman Scattering Signals for Biosensing and Bioimaging Applications *ACS Central Science* **4** 277-87

[42] Han H, Huang Z and Lee W 2014 Metal-assisted chemical etching of silicon and nanotechnology applications *Nano Today* **9** 271-304

[43] Kumar R, Shukla A K, Mavi H S and Vankar V D 2008 Size-dependent Fano Interaction in the Laser-etched Silicon Nanostructures *Nanoscale Research Letters* **3** 105

Figure captions

Figure 1. Schematic representation of the nPSi-Ag composite layers: a) synthesis of nPSi substrate by photoassisted electrochemical etching and stabilization by chemical oxidation, b) Ag deposition onto nPSi by cyclic dip-coating (CDC), and c) Ag deposition onto nPSi

by cyclic spin-coating (CSC). For both techniques, the same Ag stem-solution was used, and after the required cycles deposition performed, samples were immersed into an ascorbic acid solution.

Figure 2. FESEM images of the typical nPSi layer used in this study: a) surface and b) cross-sectional view.

Figure 3. Surface and cross-sectional FESEM images of a typical nPSi-Ag composite layer after 12-cycles deposition using CDC (a-d), and CSC (e-h). Histograms of particle size distribution: i) length in CDC, j) length in CSC, k) width in CDC, and l) width in CSC.

Figure 4. Relative concentration profile of Ag in the cross-section of nPSi-Ag composite layers obtained by SEM-EDX: a) CDC and b) CSC.

Figure 5. RBS spectrum of typical nPSi-Ag composite 471 layers fabricated by CDC and CSC after 12 cycles.

Figure 6. In-depth concentration profile of obtained by simulation of nPSi-Ag composite layers fabricated by (a) CDC and (b) CSC after 12 cycles.

Figure 7. XRD pattern of nPSi-Ag composite layers after 3, 6, 9, and 12 Ag deposition cycles using a) CDC and b) CSC. c) The difference in the intensity of the Ag (111) peak between CDC and CSC after 12 cycles of Ag deposition.

Figure 8. Raman spectra for the nPSi-Ag composite layers after 3, 6, 9 and 12 Ag deposition cycles using a) CDC and b) CSC.

Figure 9. Raman shift of the silicon one-phonon line for the nPSi-Ag composite layers after 3, 6, 9 and 12 Ag deposition cycles using a) CDC and b) CSC.

Figure 10. Intensity distribution ($|E/E0|4$) of induced electrical field determined by FDT calculations of **a)** *x-z* plane and **b)** *y-z* plane. **c)** Intensity distribution in the middle of the

nanogap as a function of the distance from the center of Ag nanoflake, for different diameters.

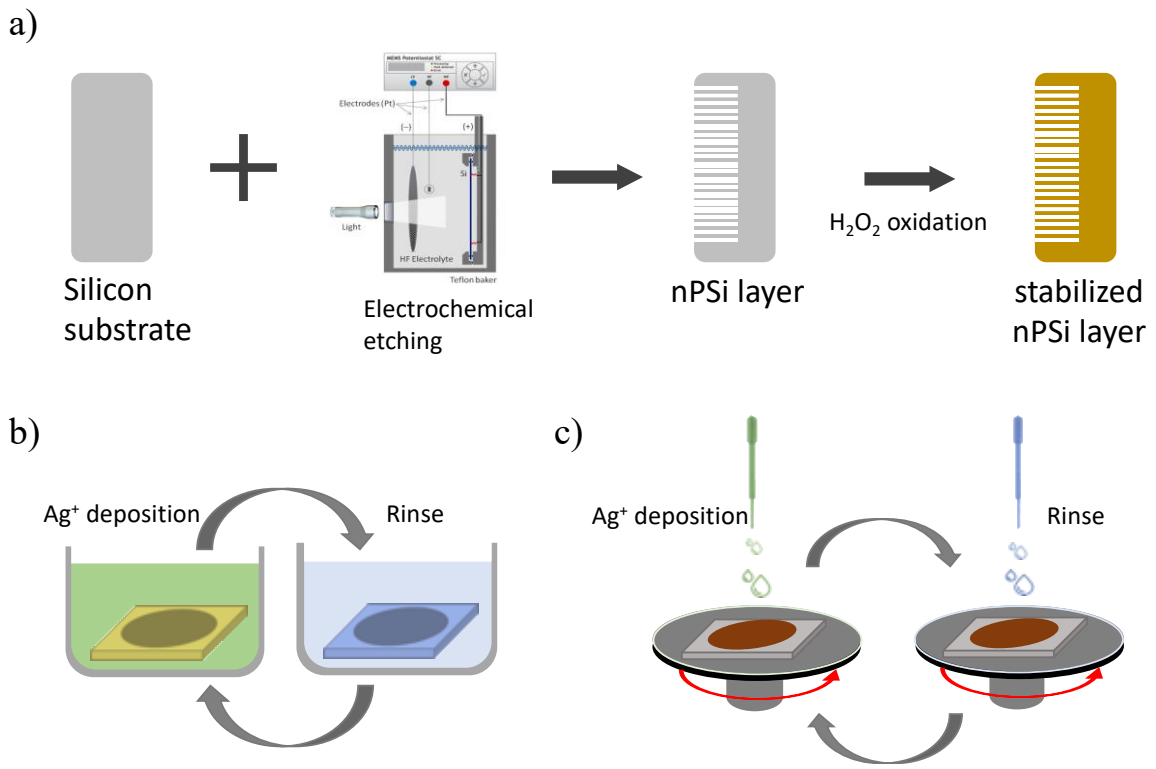

Figure 1. Schematic representation of the nPSi-Ag composite layers: a) synthesis of nPSi substrate by photoassisted electrochemical etching and stabilization by chemical oxidation, b) Ag deposition onto nPSi by cyclic dip-coating (CDC), and c) Ag deposition onto nPSi by cyclic spin-coating (CSC). For both techniques, the same Ag stem-solution was used, and after the required cycles deposition performed, samples were immersed into an ascorbic acid solution.

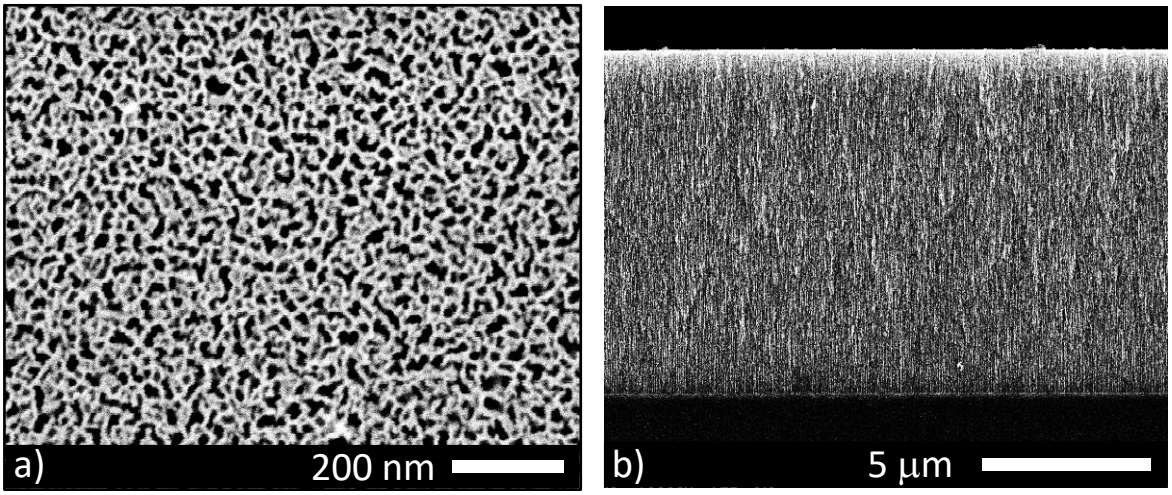

Figure 2. FESEM images of the typical nPSi layer used in this study: a) surface and b) cross-sectional view.

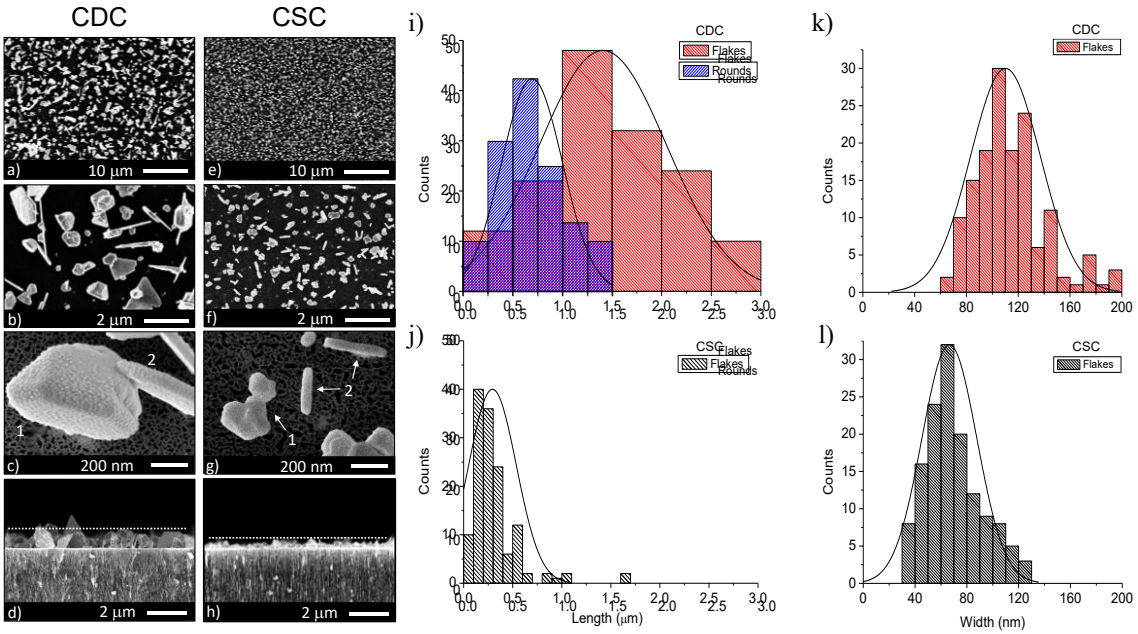

Figure 3. Surface and cross-sectional FESEM images of a typical nPSi-Ag composite layer after 12-cycles deposition using CDC (a-d), and CSC (e-h). Histograms of particle size distribution: i) length in CDC, j) length in CSC, k) width in CDC, and l) width in CSC.

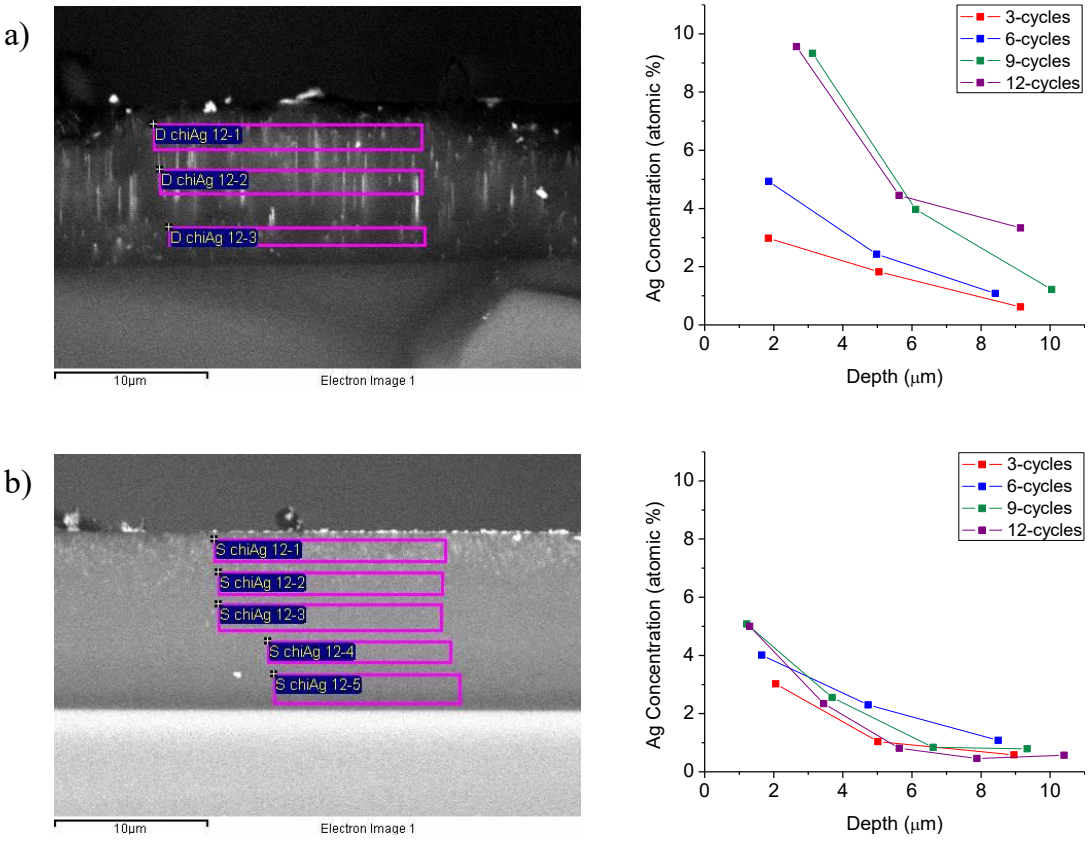

Figure 4. Relative concentration profile of Ag in the cross-section of nPSi-Ag composite layers obtained by SEM-EDX: a) CDC and b) CSC.

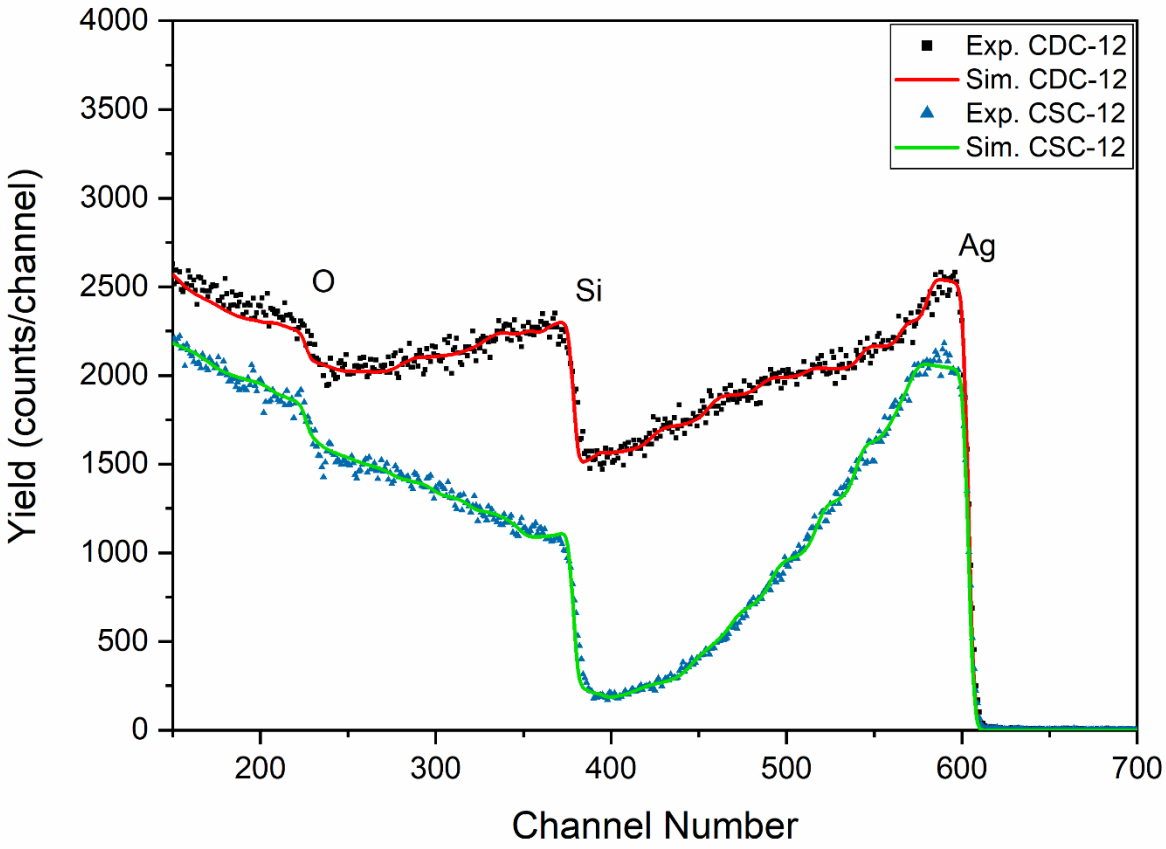

Figure 5. RBS spectrum of typical nPSi-Ag composite layers fabricated by CDC and CSC after 12 cycles.

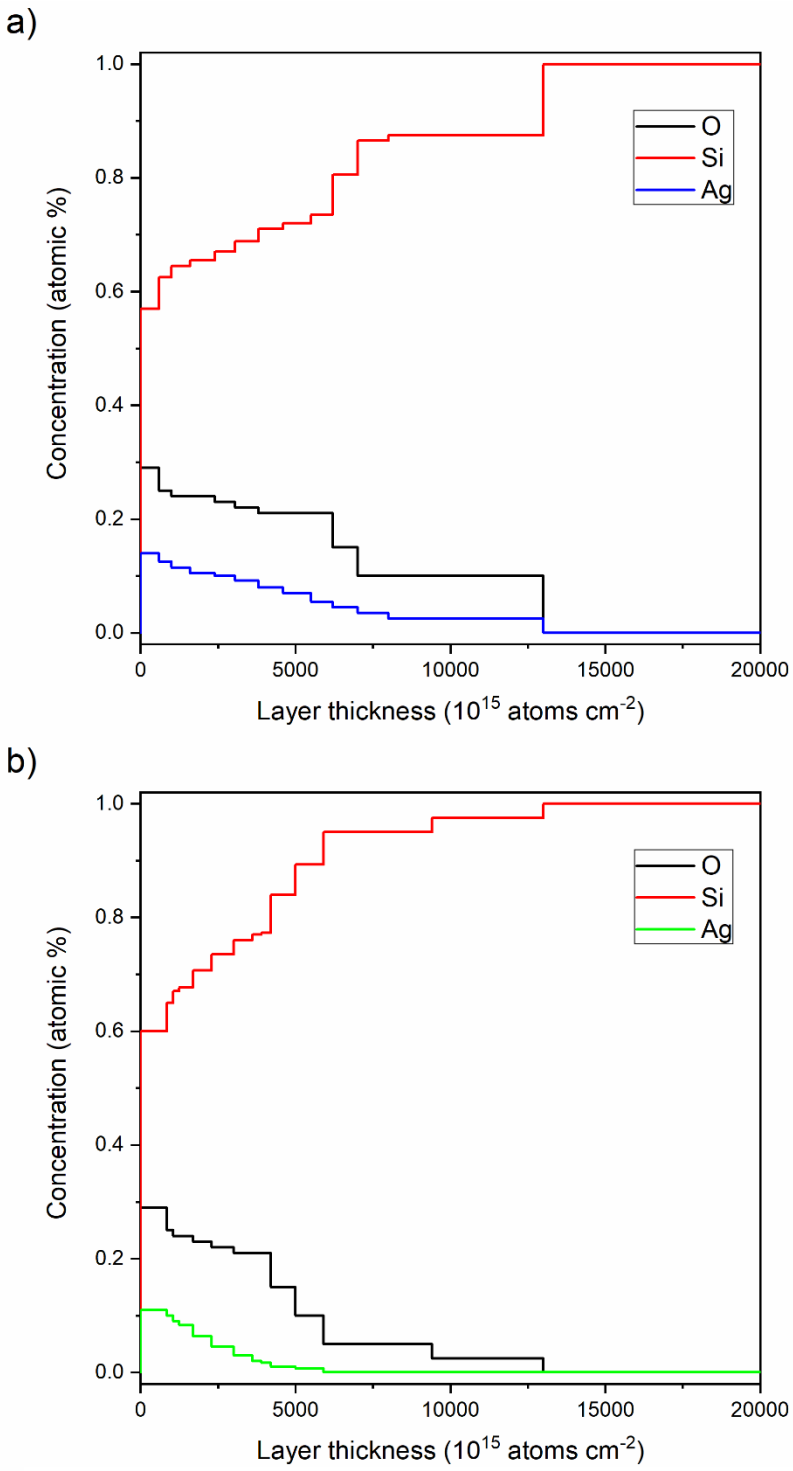

Figure 6. In-depth concentration profile of obtained by simulation of nPSi-Ag composite layers fabricated by (a) CDC and (b) CSC after 12 cycles.

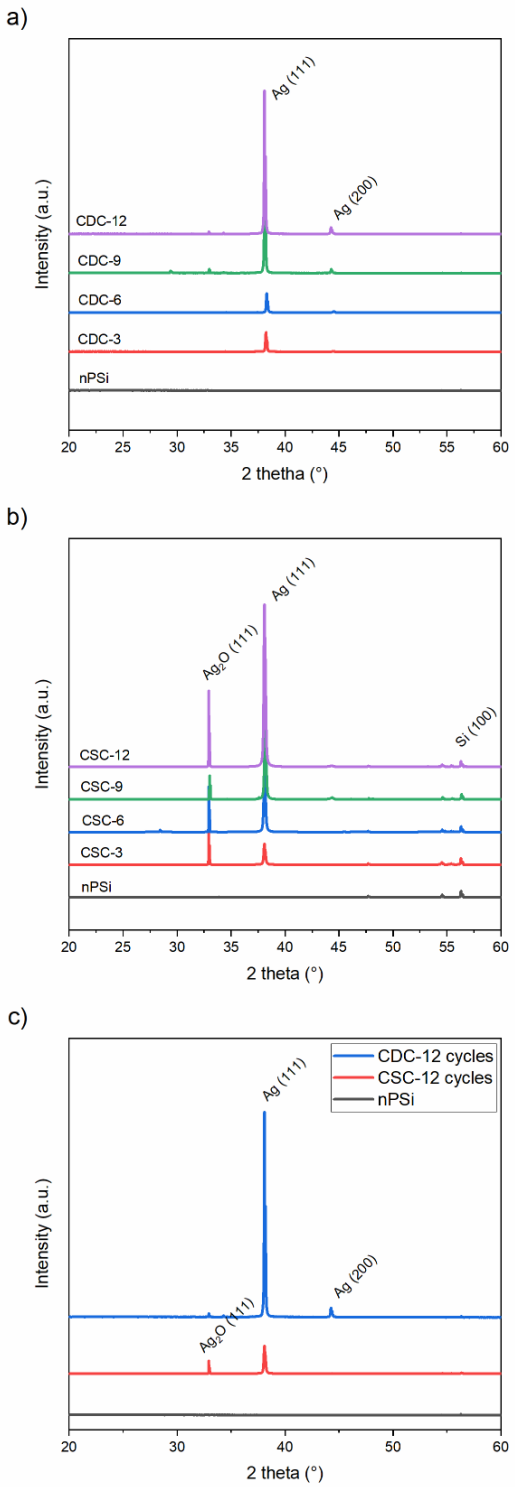

628

629 **Figure 7.** XRD pattern of nPSi-Ag composite layers after 3, 6, 9, and 12 Ag deposition

630 cycles using a) CDC and b) CSC. c) The difference in the intensity of the Ag (111) peak

631 between CDC and CSC after 12 cycles of Ag deposition.

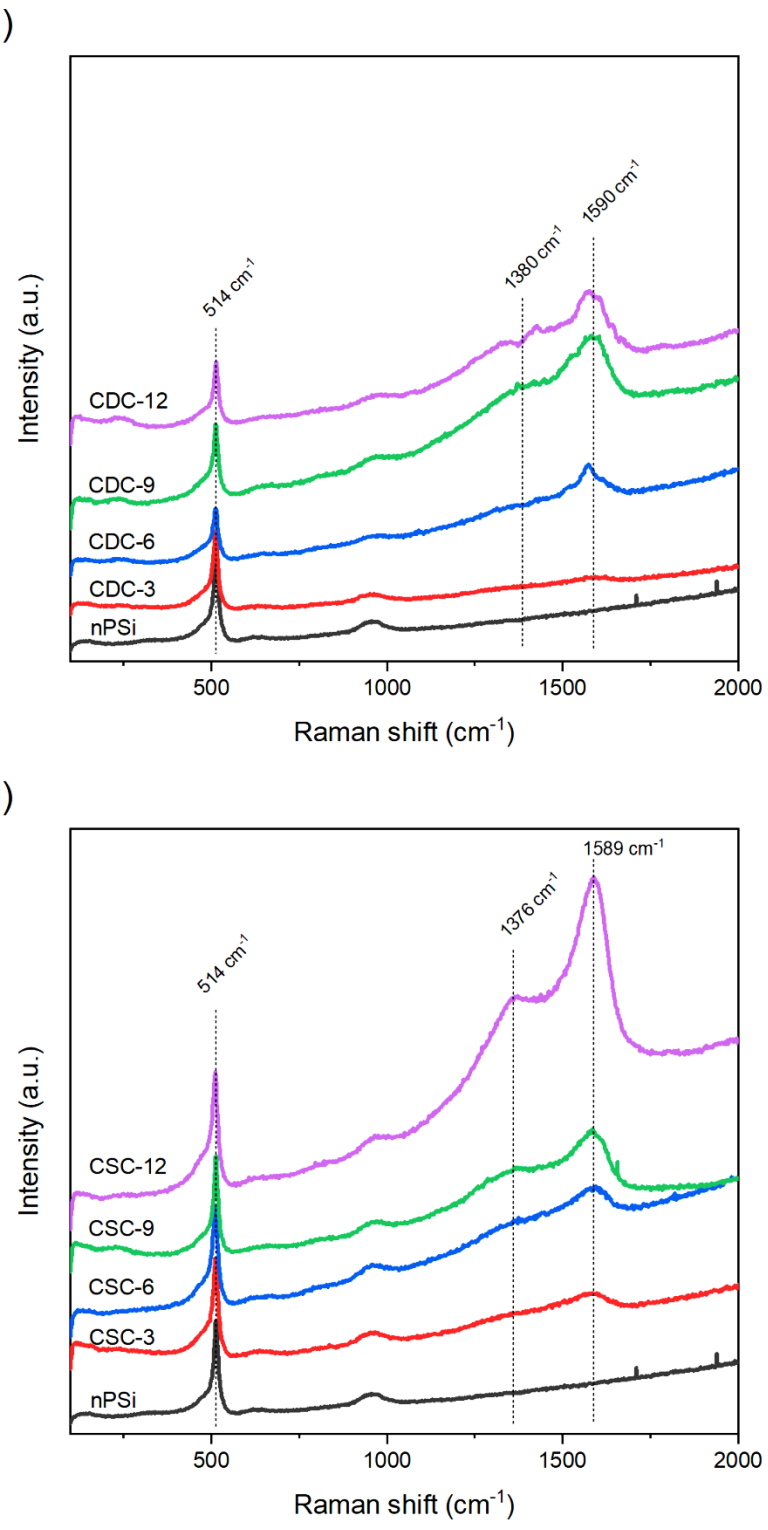

Figure 8. Raman spectra for the nPSi-Ag composite layers after 3, 6, 9 and 12 Ag deposition cycles using a) CDC and b) CSC.

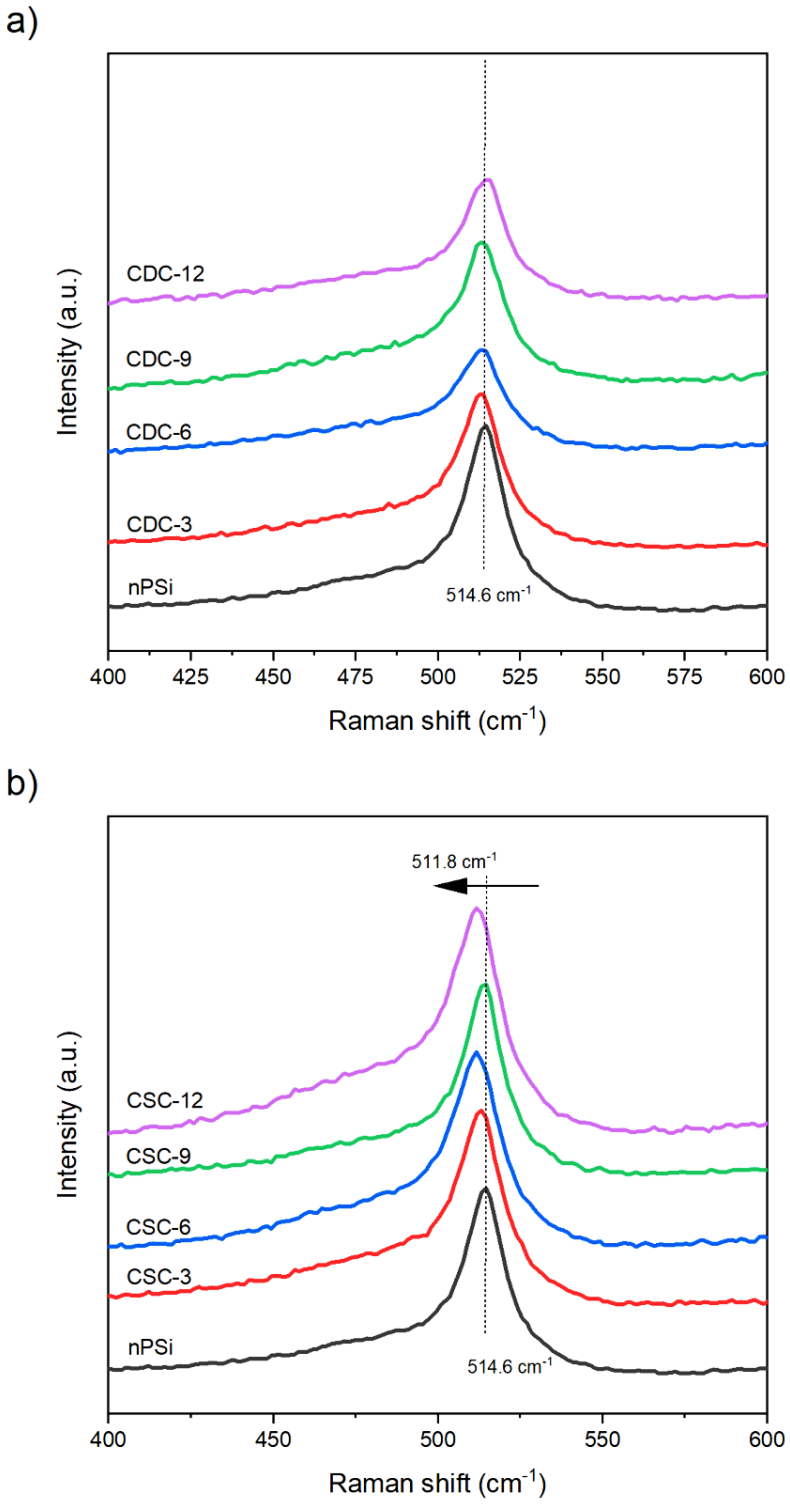

Figure 9. Raman shift of the silicon one-phonon line for the nPSi-Ag composite layers after 3, 6, 9 and 12 Ag deposition cycles using a) CDC and b) CSC.

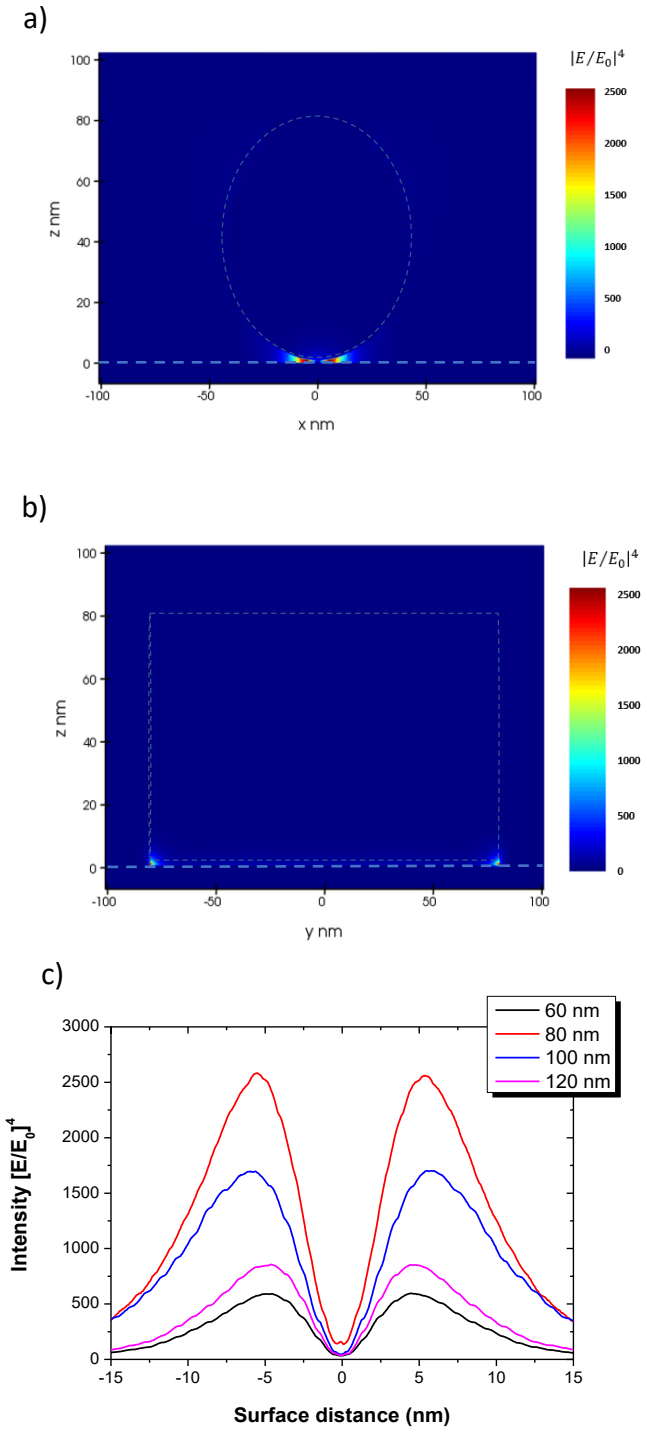

Figure 10. Intensity distribution ($|E/E_0|^4$) of induced electrical field determined by FDTD calculations of **a)** *x-z* plane and **b)** *y-z* plane. **c)** Intensity distribution in the middle of the

nanogap as a function of the distance from the center of Ag nanoflake, for different diameters.